Combustion and Flame 203 (2019) 92–104

Contents lists available at ScienceDirect

Combustion and Flame

journal homepage: www.elsevier.com/locate/combustflame

Statistics and topology of local flame–flame interactions in turbulent flames

Ankit Tyagi[a], Isaac Boxx[b], Stephen Peluso[a], Jacqueline O'Connor[a,*]

[a] Mechanical and Nuclear Engineering, Pennsylvania State University, University Park, PA, USA
[b] German Aerospace Center (DLR), Stuttgart, Germany

ARTICLE INFO

Article history:
Received 10 August 2018
Revised 1 October 2018
Accepted 5 February 2019
Available online 15 February 2019

Keywords:
Turbulent flames
Interacting flames
Flame–flame interactions

ABSTRACT

Flame–flame interaction events occur frequently in turbulent premixed flames and change the local structure and dynamics of flames. It is essential to understand these flame–flame interaction events to develop high-fidelity combustion models for use in modern combustion devices. In this study, we experimentally investigate the topology of flame–flame interaction events in single- and multi-flame configurations. A dual-burner experiment is probed with high-speed OH-planar laser-induced fluorescence and stereoscopic-particle image velocimetry to obtain simultaneous flame front locations and velocity fields. A non-rigid image registration technique is implemented to track the topological changes occurring in these flames. In both single- and dual-flame configurations, small-scale interactions occur more frequently compared to large-scale interactions, and statistics show that most of the reactant-side interactions contribute to large flame surface destructions than the product-side interactions. It is also found that turbulence length- and velocity-scales can play an important role in facilitating the interaction events and pocket formations from these events. Filamentarity is used to quantify the two-dimensional shape of these interactions and comparisons are made between the orientation and shape of interaction events and the local turbulence in the flowfield. Alignment between the orientation of the interaction shapes and the principal strain rates show that compressive fluid forces drive both types of interaction events.

1. Introduction

Interaction between turbulent flames exists in many modern combustion devices, including land-based and aircraft gas turbine combustors, jet augmenters, furnaces, and boilers. For these devices, robust prediction of system operability using numerical simulations requires understanding the behavior of multiple-flame configurations to develop high-fidelity combustion models. The stability and dynamics of these multiple flame configurations have been studied in the past [1–12]. These studies have shown that individual flames can interact with each other at a macro-level, changing global flame characteristics and device operation of these devices. Macro-level interactions typically occur where interaction of underlying flowfields of individual flows takes place, such as closely spaced arrays of injectors/nozzles or other flame holding devices like bluff-bodies. Studies conducted by Samarasinghe et al. [1,13] and Worth and Dawson [2–4] have shown that interacting flames change the distribution of heat release in multi-nozzle combustors, changing their thermoacoustic response. This flow interaction also changes the flame structure and flame attachment characteristics, impacting flame stability [14]. While these macro-level interactions are important for understanding static and dynamic stability of these flames, interactions on much smaller length-scales play a crucial role in changing the local structure of flames at a range of length-scales. These interactions, referred to as 'local flame–flame interactions' in this study, are commonly observed in turbulent premixed flames in various configurations, and the current study focuses on understanding the impact of these interactions on flame structure and propagation.

Several studies in the past have explored the characteristics of local flame–flame interactions and how they impact the behavior of the flame [15–33]. Two broad categories of local flame–flame interactions have been found to occur in turbulent premixed flames: normal interactions and counter-normal interactions [22,23]. Normal interactions, also referred to as 'reactant-side interactions', occur when two flame fronts propagate towards each other. These normal interactions can be of three types: convex interactions, tunnel closures, and pocket burnouts. Convex interactions occur when reactant gases that are surrounded by flame cusps are consumed. In tunnel closure events, a tunnel-like structure is formed and reactant gases are consumed in the middle. Pocket burnouts occur in closed forms, leading to local flame extinction [22,23,32].

* Corresponding author.
E-mail address: jxo22@psu.edu (J. O'Connor).

https://doi.org/10.1016/j.combustflame.2019.02.006
0010-2180/

Nomenclature

DNS	Direct Numerical Simulation
FOV	Field-of-view
FSD	Flame Surface Density
LES	Large Eddy Simulation
PLIF	Planar-Laser Induced Fluorescence
RANS	Reynolds-Averaged Navier–Stokes
s-PIV	Stereoscopic-Particle Image Velocimetry
$A_{\tilde{c}}$	Time-averaged flame area based on $\tilde{c}$
H	Time-averaged flame height
L_{11}	Integral length-scale in x-direction
L_{22}	Integral length-scale in y-direction
L_{-}	Arc-length of consumed flame edge
L_{+}	Arc-length of remaining flame edge
Le	Lewis number
P	Perimeter of flame–flame interaction shape
Re_w	Width-based bulk flow Reynolds number
Re_h	Hydraulic diameter-based Reynolds number
$Re_{L_{11}}$	Turbulent Reynolds number
S_T	Turbulent flame speed
$S_{T,GC_{\tilde{c}}}$	Turbulent global consumption speed based on $\tilde{c}$
S	Flame spacing
S_a	Two-dimensional surface area of flame–flame interaction shape
S_{11}	Strain rate in x-direction
S_{12}	Shear component of strain rate tensor
S_{22}	Strain rate in y-direction
U	Bulk flow velocity
W	Burner width
$\tilde{c}$	Time-averaged progress variable
l_f	Laminar flame thickness
$\dot{m}_R$	Mass flow-rate of reactants
s_L	Unstretched laminar flame speed
u'	Turbulence velocity-scale
u'_x	x-component of turbulence velocity scale
u'_y	y-component of turbulence velocity scale
u'_z	z-component of turbulence velocity scale
x	Stream-wise direction
y	Cross-stream direction
z	Span-wise direction
ρ_R	Density of reactants
θ_b	Angle between flame–flame interaction shape and y-axis
θ_p	Principal strain angle
ϕ_b	Angle between major and minor axes vectors of flame–flame interaction shape
λ_{Taylor}	Taylor length-scale
$\Delta\theta$	Angle difference between θ_b and θ_p
$\mathcal{F}$	Filamentarity
$\mathcal{R}_R$	Reactant-side interaction rates
$\mathcal{R}_{R_{pocket}}$	Pocket formations from reactant-side interactions
$\mathcal{R}_P$	Product-side interaction rates
$\mathcal{R}_{P_{pocket}}$	Pocket formations from product-side interactions

Counter-normal interactions, also referred to as 'product-side interactions', occur when the product sides of flame fronts interact and studies have shown that a highly strained flowfield is necessary for these interactions to occur [15,21–23,31,32].

Local flame–flame interactions impact the local structure of the flame due to interactions occurring between the preheat zone, the inner layer, and the oxidation layer [19,20]. Heat and species distributions change in the interaction region, leading to changes in flame propagation. A direct numerical simulation (DNS) study conducted by Chen and Sohrab [16] showed that for normal interactions, the gradients of radical species and temperature in the interaction region change due to the merging of the preheat zones during the interaction. As a result, transport of species and temperature across these zones affects the flame propagation speed. Additionally, the frequency of flame interactions is dependent on Lewis number (Le), as shown by Dunstan et al. [23] and Im and Chen [17]. Non-unity Lewis numbers can result in either preheating (for $Le > 1$) or species doping (for $Le < 1$) of the reactant mixture in interaction regions. Im and Chen investigated H_2–air flames and found that fuel-rich interacting flames ($Le > 1$) show instances where flames pinch, form cusps, and display rapid kinematic restoration after the interaction, reducing local curvature. Fuel-lean interacting flames ($Le < 1$) experience thermo-diffusive instabilities, where flame interactions lead to growth of regions with high curvatures. These instabilities result in high flame stretch, which leads to flame quenching and more product-side interactions.

Changes in flame area due to flame–flame interactions can dynamically change the overall flame behavior. Dunstan et al. [22,23] calculated changes in global stretch rates and decomposed the global stretch rate into turbulence–flame and flame–flame interaction components. Interactions were found to cause global stretch rates to deviate to negative values, primarily due to the flame–flame interaction component. The rapid fluctuations in flame area and flame stretch from flame–flame interactions also affect flame speed. Chen et al. [28] showed that the density-weighted displacement speed increases by a factor of four during a pocket burnout event due to local preferential diffusion effects. Similarly, flame propagation speeds and consumption speeds have been shown to increase during interaction events in other studies [16,19,20,27]. Many of these studies focused on the behavior of individual events; those with statistically-converged data on interaction populations typically used over-simplified chemistry to make the DNS tractable. While DNS studies accurately capture interactions and their impact on flame structure and propagation, there has been little work linking the interaction topologies to the flowfield in real turbulent flame configurations. Additionally, DNS is a computationally expensive technique to use for studying the sensitivity of these interactions to variation in operating conditions.

Less expensive techniques, such as Reynolds-Averaged Navier–Stokes (RANS) and Large Eddy Simulation (LES), are more commonly used to simulate laboratory and industrial-scale flames; however, some of these techniques rely on modeling the flame behavior at sub-grid scales. A commonly-used sub-grid turbulent combustion model uses flame surface density (FSD) transport equations [34–40], where the turbulent flame speed directly correlates with FSD [35,41] and appropriate modeling of FSD at the sub-grid scale requires the knowledge of flame surface generation and destruction mechanisms. In these models, flame surface destruction is attributed to reduction in flame area due to quenching and mutual flame–flame interactions [35]. Various models have been proposed to account for this phenomenon [34,36], although very limited experimental measurements have been performed for validation of these models. Skiba et al. [42] used high-speed CH-PLIF imaging of reaction layers to experimentally quantify the merging rate of flamelets to provide some insights on the destruction rate of FSD in a round Bunsen turbulent flame. There were uncertainties in the interaction identification algorithm in their study, and results were limited to only one operating condition.

The goal of this work is to experimentally characterize the frequency and topology of local flame–flame interaction events at a range of operating conditions in both single- and dual-flame configurations in a modular burner experiment, motivated by the need for better understanding of flame annihilation processes for FSD models. Optical diagnostics and image processing techniques

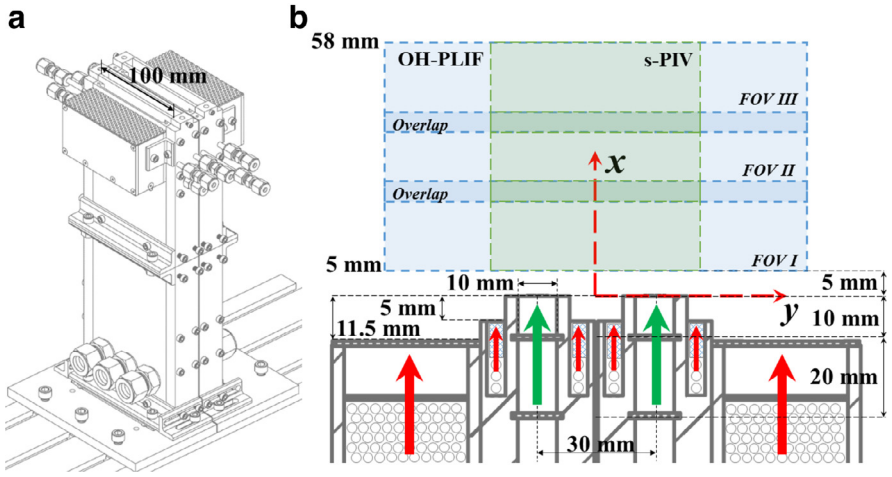

Fig. 1. Schematic of the dual burner setup and fields-of-views (FOVs) for optical measurements. In figure (b), the red arrows represent the flow path for the pilot flame premixed gases and the green arrows represent the flow path for the main flame premixed gases. (For interpretation of the references to color in this figure legend, the reader is referred to the web version of this article.)

are implemented on a variety of data sets to obtain simultaneous velocity and flame edge statistics to link the flame morphology with the local turbulent flow behavior. To illustrate the impact that local interactions have on the flame structure, we characterize both the local flame and flow structure, linking the two to show how turbulence-flame interactions drive flame–flame interactions. Quantification of the frequency of these flame–flame interactions is presented as it directly correlates with the flame surface destruction rate that is required for sub-grid scale FSD models. We also provide data on flame surface annihilation at a range of conditions. Insights into topologies of the interactions are also provided to show how the local flow behavior can change the size and shape of interactions, which may need to be accounted for in the flame surface destruction models. The outcome of this work is a better quantification of the frequency of these interactions and an elucidation of what is driving them to occur at a range of operating conditions.

2. Experimental configuration

2.1. Burner configuration

The experimental facility consists of two identical burners mirrored about the experiment centerline with rectangular exit planes of dimensions 100 mm × 10 mm (Fig. 1). Each burner contains the inlet for the premixed reactants (natural gas and air), two ceramic honeycomb flow-straighteners, and two perforated-plate turbulence generators. These plates have 3.2 mm hole-diameters, 40% open area, and are mounted 30 and 10 mm upstream of the burner exit. The plates are designed to produce a uniform turbulent flow at the burner exit and are specified according to empirical correlations [43]. The inlet temperature for the premixed reactants is approximately 300 K and the flames are operated at 1 atm. Each burner is also equipped with two types of pilot flames, operated at stoichiometric conditions, along the 100 mm side of the slot: small 'anchoring' pilots, which are located close to the exit of the burners and help stabilize atmospheric pressure flames on the experiment, and larger 'back-support' pilots, which provide adiabatic or super-adiabatic combustion products around the flames. The anchoring pilots have a narrow rectangular exit plane with dimensions of 90 mm × 4.8 mm, located 5 mm upstream of the burner exit plane. The back-support pilots also consist of rectangular exit planes with dimensions 90 mm × 30 mm, located 11.5 mm upstream of the burner exit plane. The burners are mounted to a two-axis translation stage, which allows for changing fields-of-view (FOVs) for laser measurements. The dual burner setup can be changed to a single burner setup by attaching the back-support pilot flames of the right burner as a secondary pilot to the left burner to make the flow configuration symmetric on the left burner.

Table 1 shows the text matrix used in this study. The equivalence ratios for main flames and pilot flames are set to unity. For cases A–E in Table 1, the bulk velocities are varied from 12 to 28 m/s in increments of 4 m/s, while the flame spacing is kept constant at 30 mm (the closest spacing possible). Additionally, measurements at single-flame configurations are performed for cases A, C, and E to make direct comparisons between single- and dual-flames. For cases F–I, the bulk velocity is kept constant at 20 m/s while the flame spacing is varied from 35 to 50 mm in 5 mm increments. All the flames in Table 1 operate in the thin-reactions regime on the Borghi–Peters' premixed combustion regime diagram [44].

2.2. Diagnostics and data processing

2.2.1. OH-planar laser induced fluorescence (OH-PLIF)

High-speed planar laser induced fluorescence (PLIF) was used to measure the distribution of the hydroxyl combustion radical in the post-combustion products. This 10 kHz acquisition-rate system consists of a 532 nm Nd:YAG laser (Edgewave) pumping a dye laser (Sirah Credo). The dye laser is tuned to the $Q_1(6)$ line of the $A^2\ \Sigma^+ \leftarrow X^2\ \Pi$ (1-0) excitation band to excite OH radicals with a wavelength of 282.94 nm. The maximum pulse energy obtained from the dye laser at 10 kHz repetition-rate is 0.3 mJ/pulse and the final collimated sheet has an approximate height of 21 mm. A CMOS sensor camera (Photron FASTCAM SA1.1), coupled with an external intensifier (LaVision HS-IRO) and a 100 mm f/2.8 UV lens (Cerco) is used with a high transmissivity interference filter (LaVision 1,108,760 VZ) to collect the signal at 320 nm. The field of view achieved through this setup is 50 mm × 100 mm. The intensifier gate is set at 100–150 ns to reduce background flame luminosity. The resulting image resolution is 0.1 mm/pixel. 5000 images are acquired for simultaneous OH-PLIF/s-PIV measurements and 10,000 images are acquired for only OH-PLIF measurements.

2.2.2. Stereoscopic-particle image velocimetry (s-PIV)

A high-repetition-rate, dual cavity, Nd:YAG laser (Quantronix Hawk Duo) operating at 532 nm is utilized to perform stereoscopic-particle image velocimetry at 10 kHz in forward

Table 1
Flow conditions of burners.

Case	Bulk flow properties			Non-reacting inlet turbulence characteristics						S [mm]	Simultaneous measurements
	U [m/s]	Re_w	Re_h	u' [m/s]	L_{11} [mm]	λ_{Taylor} [mm]	$Re_{L_{11}}$	u'/s_L	L_{11}/l_f		
A-Dual	12	8500	15,000	2.2	2.1	1.4	325	5.5	11.1	30	Yes
A-Single										–	No
B-Dual	16	11,000	21,000	2.9	2.4	1.3	484	7.2	12.5	30	No
C-Dual	20	14,000	26,000	3.6	2.3	1.3	575	8.9	11.8	30	Yes
C-Single										–	No
D-Dual	24	17,000	31,000	4.3	2.2	1.3	687	10.7	11.8	30	No
E-Dual	28	19,000	36,000	5	2.2	1.2	787	12.4	11.6	30	Yes
E-Single										–	No
F-Dual	20	14,000	26,000	3.6	2.3	1.3	575	8.9	11.8	35	No
G-Dual	20	14,000	26,000	3.6	2.3	1.3	575	8.9	11.8	40	Yes
H-Dual	20	14,000	26,000	3.6	2.3	1.3	575	8.9	11.8	45	No
I-Dual	20	14,000	26,000	3.6	2.3	1.3	575	8.9	11.8	50	Yes

scatter mode. The final height of the collimated laser sheet is 50 mm. A pair of CMOS sensor cameras (Photron FASTCAM SA5) equipped with 100 mm f/2.8 lenses (Tokina Macro) and Nikon teleconverters are used to accommodate for a safe stand-off distance between the cameras and the burners, without compromising the resolution and the field of view. The angle between the laser sheet plane and each camera sensor is about 25 degrees. The field of view obtained through this setup is 32 mm × 53 mm. The flowfield is seeded with 0.5–2 μm sized aluminum oxide particles, and 532 nm laser-illuminated images are collected at 10 kHz in a double frame mode, with a pulse separation of 14 μs. Based on a 1 μm nominal diameter of these particles, the particle Stokes number is approximately 0.06, which means that the particle can track flow oscillations up to 4000 Hz [45]. Near-infrared filters and laser line filters are utilized to filter the signal before it is collected on the camera sensor. Vector calculations from the collected images are performed using DaVis 8.3 from LaVision. A multi-pass algorithm is used with window sizes ranging from 64 × 64 to 16 × 16; for each pass, a 50% overlap is used. The resulting vector spacing is 0.48 mm/vector. Post-processing of vectors is performed with a universal outlier detection scheme, with a 3x median filter. Using the uncertainty calculation feature in DaVis 8.3, averaged uncertainties in instantaneous velocities range from 1.4 to 2.5 m/s in the jet region of the burners for U=12–28 m/s. 5000 vector fields are obtained for cases with simultaneous OH-PLIF/s-PIV measurements (Table 1).

Figure 2 shows the layout of the simultaneous OH-PLIF and s-PIV system. Synchronization of the OH-PLIF and s-PIV systems is performed using Stanford Research Systems DG-535 digital delay generators. The UV laser pulse for the OH-PLIF system is placed between the two s-PIV laser pulses at an offset of 10 μs from the first 532 nm pulse.

2.2.3. Flame front identification and image registration

The OH-PLIF images are binarized using a dynamic thresholding technique that reduces the sensitivity of the calculation to intensity variations in each frame. Images are corrected for laser sheet profile variations using a signal profile taken in a region of steady, homogenous OH generated by the laminar pilot flames; the profile is comprised of the average of 1000 images. Median and bilateral filters are applied to the sheet corrected images to remove speckle noise and smooth discrete intensity changes. Otsu's method [46] is used to perform thresholding to obtain a binarized image. The flame edges are obtained by tracing the edges of the binarized images using the '*bwboundaries*' function in MATLAB [46]. Impact of the thresholds of this binarization method are discussed in the supplementary material. Time-averaged progress variable field ($\tilde{c}$) is obtained by calculating the average of all binarized images obtained for each case, where reactants have a progress variable of 0 and products a progress variable of 1.

A non-rigid image registration technique [22,23] is utilized to identify local flame–flame interaction events. This technique estimates non-uniform displacement fields to perform image alignment between two binarized OH-PLIF images [47–50]. A detailed discussion of this technique and the uncertainties associated with it are included in the supplementary material, but a brief description of its implementation is provided here. Schematics of interaction events identified from the image registration technique are shown in Fig. 3. Once consecutive binarized OH-PLIF images are registered, they are subtracted to search for non-zero regions that correspond to topological changes occurring within 100 μs between frames. Edges of the non-zero regions (regions with hashed pattern in Fig. 3) are evaluated and decomposed into L_- and L_+. Here, L_- identifies the part of the flame edge that is consumed due to the interaction event and L_+ is the part that remains on the connected flame edge after the interaction occurs. For all non-zero regions identified, comparisons between the arc-lengths of L_- and L_+ are made to ensure only flame surface reduction events are captured. These post-processing steps are taken for both reactant- and product-side interactions separately. To isolate the influence of existing flame pockets on attached flame fronts and merging/breaking of flame pockets, topological differences due to merging of flame pockets on attached flame fronts are not counted in the interaction statistics. Flame–flame interactions obtained from this analysis are referred to as "attached" flame–flame interactions. Additionally, non-zero regions comprising of 25 pixels or less are excluded to avoid registering non-physical topological changes as a flame–flame interaction. This filtering results in the smallest identified flame surface destruction region to have a perimeter of 1.77 mm. Assuming a flame extinction velocity of 2 m/s for a laminar methane-air flame at 300 K and 1 atm, the time-scale to resolve this annihilation is approximated to be 885 μs, which is well above the sampling time step of 100 μs. Annihilation events occurring at much smaller time-scales are not captured with this setup. More details on the sensitivity of interaction events on sampling rate are provided in the supplementary material.

2.2.4. Turbulence length-scale calculations

Turbulence length-scales are calculated using vector fields conditioned on locations of time-averaged progress variables ($\tilde{c}$). The autocorrelation of the stream-wise velocity fluctuations are utilized to calculate the stream-wise and cross-stream integral length-scales, L_{11} and L_{22} [51]. For each pixel of a time-averaged progress variable location, autocorrelations are calculated in the x-direction to obtain L_{11}. For calculations of L_{22} at the same pixel locations, the autocorrelations are calculated in the y-direction towards the reac-

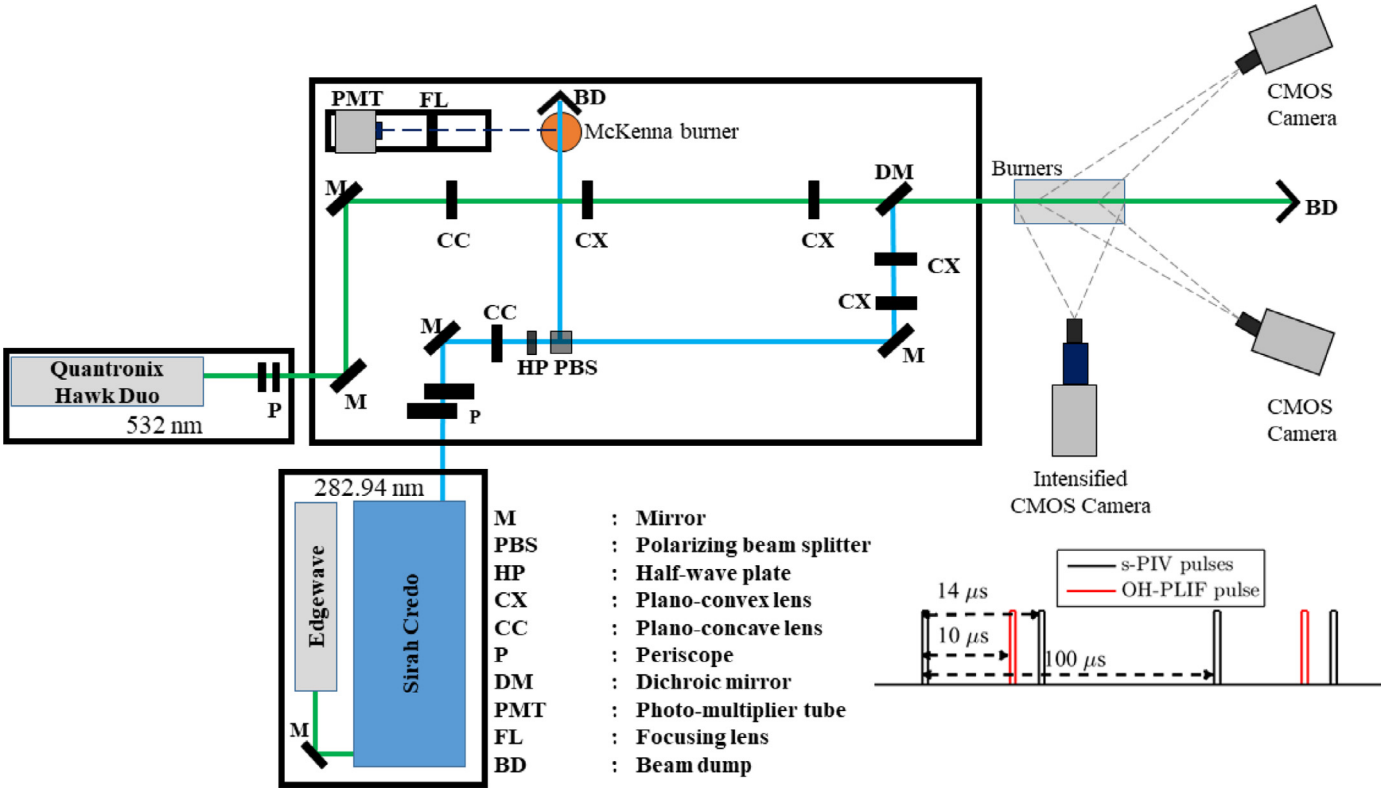

Fig. 2. Schematic of optical layout for OH-PLIF and s-PIV systems.

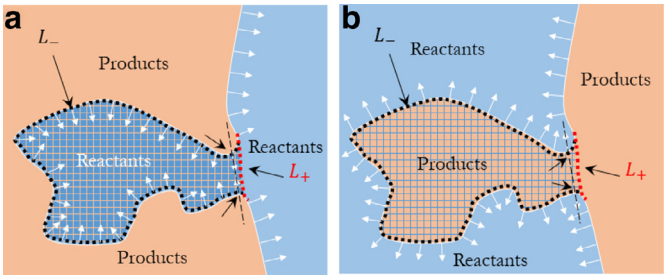

Fig. 3. Schematic of examples of (a) reactant-side and (b) product-side flame–flame interactions.

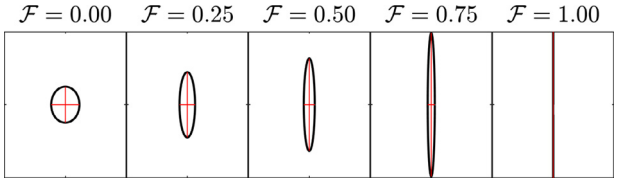

Fig. 4. Filamentarity ($\mathcal{F}$) illustration for circle to filament.

tants. The integral length-scale calculations are performed for the inner branches of each flame in the dual-flame cases. More discussion of turbulent quantity calculations is provided in the supplementary material.

2.2.5. Filamentarity of flame–flame interactions

Filamentarity ($\mathcal{F}$) is a shapefinder metric that quantifies the topology of 2D shapes using the partial Minkowski functionals—surface area S_a and perimeter P [52]. Eq. (1) is utilized to calculate the filamentarity of attached flame–flame interactions. Shown in Fig. 4 are illustrations of example shapes associated with $\mathcal{F}$ values of 0.00, 0.25, 0.50, 0.75, and 1.00. These transitioning shapes correspond to a circle morphing into a filament with equal surface area. The major-to-minor axis ratios of these shapes are: 1.0, 3.5, 7.0, 16.8, and 30734.0 and correspond to the intensity of unidirectional stretching of these shapes.

$$\mathcal{F} = \frac{P^2 - 4\pi S_a}{P^2 + 4\pi S_a} \tag{1}$$

3. Results and discussions

3.1. Global flame structure comparisons

Table 2 shows the flame heights ($H_{\bar{c}}$) of single- and dual-flame cases as described by Eq. (2). This definition is taken from [41], which approximates the height of rectangular Bunsen flames based on the burner width (W), the bulk flow velocity of the reactant flow mixture (U), and the turbulent global consumption speed ($S_{T,GC_{\bar{c}}}$) conditioned on time-averaged progress variable, $\bar{c}$. $S_{T,GC_{\bar{c}}}$ is calculated using Eq. (3), where $\dot{m}_R$, ρ_R, and $A_{\bar{c}}$ are the mass flow rate of the reactant flow mixture, the density of this mixture, and the surface area of a contour for a given $\bar{c}$, respectively [53].

$$H = \left(\frac{W}{2}\right) \times \left(\frac{U}{S_{T,GC_{\bar{c}}}}\right) \tag{2}$$

$$S_{T,GC_{\bar{c}}} = \frac{\dot{m}_R}{\rho_R A_{\bar{c}}} \tag{3}$$

Due to the limited field-of-view, we calculate the height based in a time-averaged progress variable of $\bar{c}$=0.2.

The calculated heights in Table 2 are the same for single- and dual-flame cases; the major difference in the time-averaged flame structures between these configurations can be seen in Fig. 5, which shows the stitched $\bar{c}$ of the left burner flame from three FOVs for all conditions in Table 1. For all dual-flames, the flames bend away from the centerline of the experiment in FOVs II and

Table 2
Flame heights for single- and dual-flames cases.

Case	Single-flames			Dual-flames								
	A	C	E	A	B	C	D	E	F	G	H	I
S [mm]	–			30					35	40	45	50
U [m/s]	12	20	28	12	16	20	24	28	20			
$S_{T,GC_{\bar{c}=0.2}}$ [m/s]	2.25	2.65	2.90	2.01	2.08	2.32	2.54	2.64	2.43	2.40	2.43	2.33
H [mm]	35	46	56	35	43	48	52	58	46	47	46	48

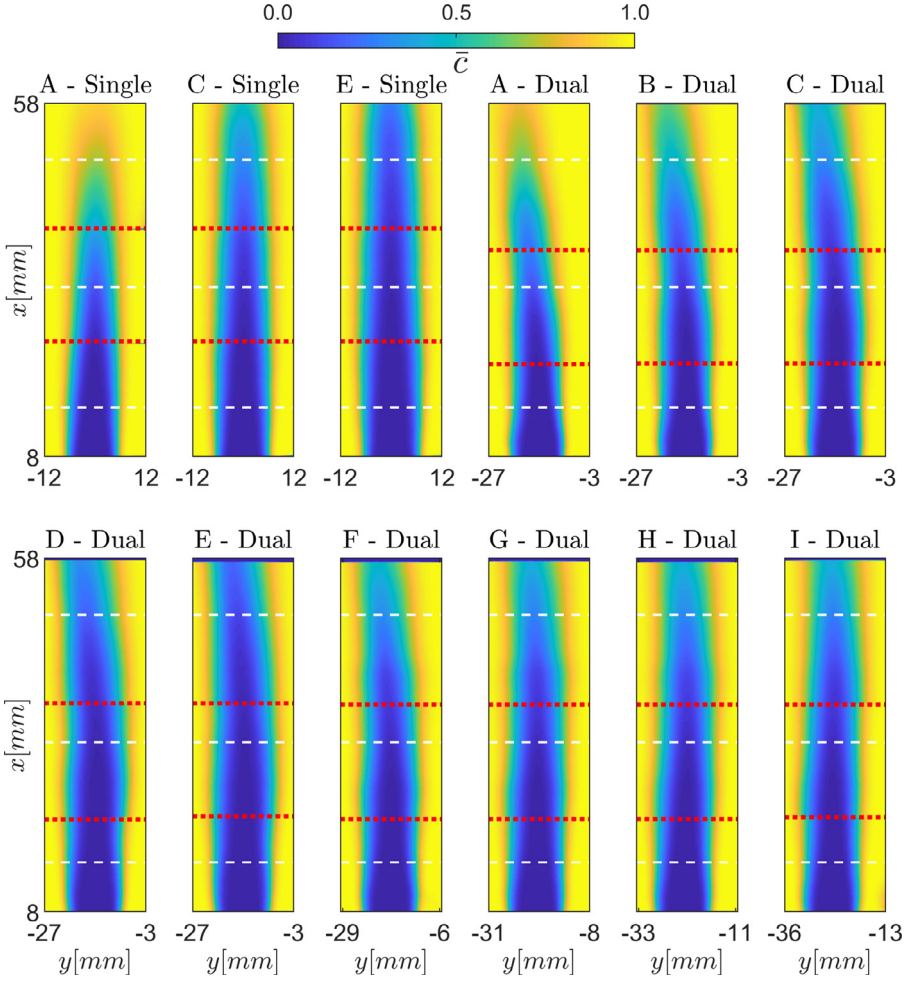

Fig. 5. Time-averaged progress variables ($\bar{c}$) of the left burner flame in single- and dual-flame configurations for the test matrix. The x-axis is limited to 8–58 mm above the burner exit for directly comparing the global flame structures between single- and dual-flames. The y-axis for each case span 24 mm centered at the left burner axis. Red dotted lines represent stitching of the FOVs. (For interpretation of the references to color in this figure legend, the reader is referred to the web version of this article.)

III, which is a result of the gas expansion occurring across the inner flame branches of both flames; the extent of the deflection is an indication of the level of interaction of the flowfields.

Figure 6 shows a comparison of horizontal slices of $\bar{c}$ at x=15, 32, and 50 mm for single- and dual-flames. The x locations here correspond to the white dashed lines in Fig.5. In Fig. 6(a), $\bar{c}$ comparisons are made between cases A, C, and E to identify the effects of variations in bulk flow velocity on the time-averaged flame structures of single- and dual-flames, showing that flame deflection is stronger in FOVs II and III for lower velocities. Figure 6(b) shows the $\bar{c}$ comparison for cases C, F, G, H, and I, where S is varied in 5 mm increments from 30 to 50 mm. This figure shows that differences in $\bar{c}$ plots are only observed near the flame tip region (FOV III for these flames) and that flow interaction effects on $\bar{c}$ are negligible for larger burner separations (S = 45 and 50 mm). While the focus of the current study is to highlight the dynamics of the local structure of single- and dual-flames, these global flame

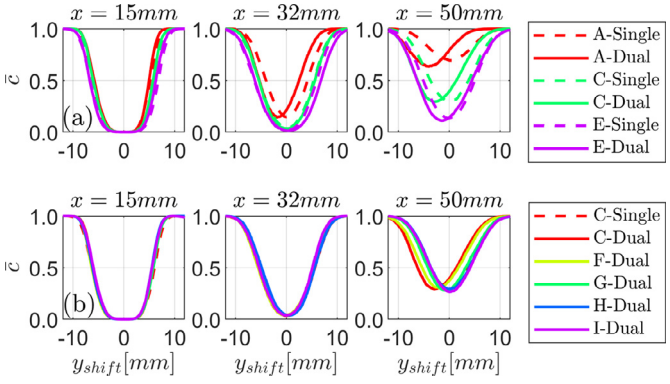

Fig. 6. Comparison of horizontal slices of $\bar{c}$ at x=15, 32, and 50 mm for single-and dual-flame (a) cases A, C and E, (b) cases C, F-I. Here, the ***y*** coordinates have been shifted to the centerline of the left burner.

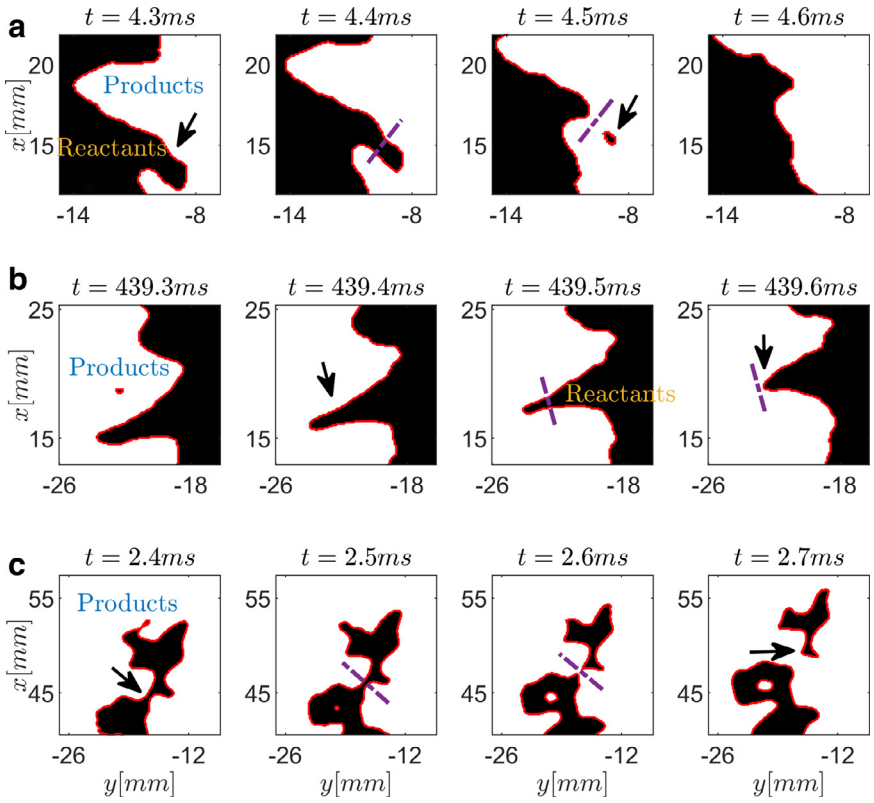

Fig. 7. Time-series of a reactant-side interactions for dual-flames case A: (a) interaction leading to reactant pocket formation in FOV I, (b) interaction without pocket formation in FOV I, and (c) interaction in the flame tip region leading to formation of large-scale pockets (note the difference in scales in each set of images). Red boundaries indicate the location of the flame front. Purple dashed lines indicate the spatial locations of the interaction events. (For interpretation of the references to color in this figure legend, the reader is referred to the web version of this article.)

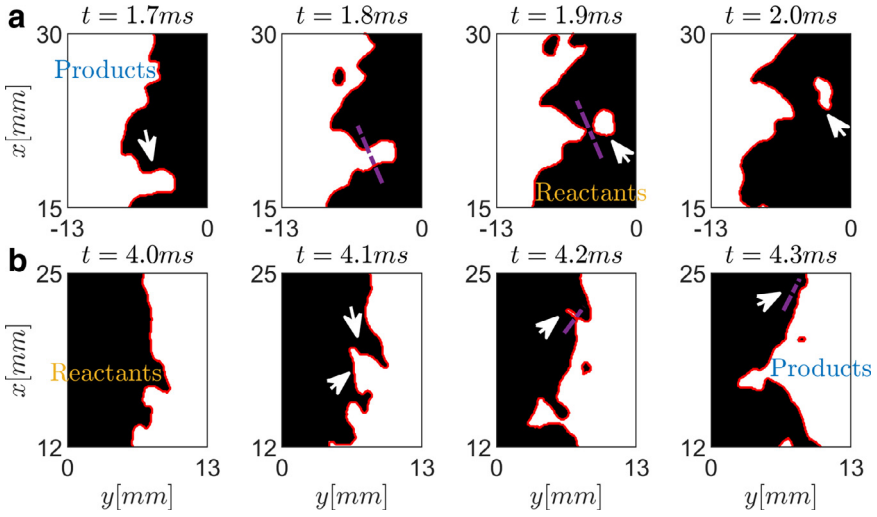

Fig. 8. Time-series of a product-side interactions for single-flame case E: (a) interaction leading to reactant pocket formation in FOV I and (c) interaction without pocket formation in FOV I. Red boundaries indicate the location of the flame front. Purple dashed lines indicate the spatial locations along the flame front of the interaction events. (For interpretation of the references to color in this figure legend, the reader is referred to the web version of this article.)

structure comparisons highlight the differences in $\tilde{c}$ distributions, which impact the progress-variable conditioned statistics.

3.2. Example cases of local flame–flame interactions

Illustrations of local flame–flame interactions are shown in Figs. 7 and 8. These cases are not intended to completely explain the dynamics of local flame–flame interaction events, but instead provide examples to orient the reader. In each of these figures, time series of binarized images and flame edges, marked in red, for local flame–flame interaction events are shown. The spatial locations of the interaction event along the flame front are marked by the purple dashed lines. As shown in Fig. 7(a)–(c), reactant-side interactions can occur in three different ways: (1) merging of local flame fronts, leading to destruction of flame surface and formation of small-scale reactant pockets, (2) merging of local flame fronts, leading only to destruction of flame surface (also known as "cusping"), and (3) merging of flame branches in the flame tip region,

leading to formation of large-scale reactant pockets (also known as "flame pinching"). In all three scenarios, flame surface destruction occurs due to flame–flame interactions ($L_- > L_+$). Additionally, cases shown in Fig. 7(a) and (c) show that flame–flame interaction events could redistribute flame surface through formation of flame pockets, which typically burn out. These interaction events lead to flame surface destruction and the range of scales over which flame surface destruction occurs can change based on the topology of these events, as highlighted by these examples.

Figure 8 shows examples of product-side interactions of two kinds: (1) merging of the local flame front, leading to a product pocket formation, and (2) merging of the local flame front, leading to the destruction of flame surface. In Fig. 8(a), the local product-sides of the flame front move toward each other, resulting in the formation of a product pocket, which convects in the free stream of reactants. However, it is unclear from planar OH-PLIF measurements whether this product region contains a reaction layer around it. Additional measurements, such as simultaneous OH/CH-PLIF, could be used to detect an active reaction layer in these regions, which is beyond the scope of this study. Despite this ambiguity, this event highlights that product-side interactions can also change flame surface density. In contrast to this example, Fig. 8(b) shows that counter-normal interactions may not necessarily lead to formation of product pockets and can sometimes result in the destruction of flame surface. Similar to the reactant-side interactions, these examples highlight that product-side interactions can occur over a range of scales.

The examples shown above do not provide a statistical overview of the interaction events occurring in turbulent premixed flames, but instead show the general categories of interaction events captured in this study. In the next few sections, results on the frequency of these interaction events and their topologies are presented to quantify the impact of flame–flame interactions on the flame surface.

3.3. Attached flame–flame interaction frequency

The frequency of flame–flame interactions is defined as the number of flame surface destruction interactions identified over a duration of measurement, reported in units of Hz. Knowing how this rate changes with operating condition and in different locations along the flame is the first step towards building a better FSD destruction model. Figure 9 shows the rates of reactant-side attached flame–flame interactions for single- and dual-flame cases at a range of bulk flow velocities (cases A-E in Table 1). Figure 9(a) and (b) shows the rates of reactant-side interactions ($\mathcal{R}_R$[Hz]) in all three FOVs. Here, the mid-point of each FOV is used to represent the downstream location and is normalized by the flame height H. In the dual-flame cases, the values of $\mathcal{R}_R$ for either flame show a maximum variability of ±10%; the interaction rates for dual-flames reported in this section are averages of the two flames. Interaction rates increase with bulk flow velocity for both configurations. The turbulence intensity for cases A–E is approximately 18%; however, the absolute turbulence level increases as the bulk flow velocity is increased. As a result, increased wrinkling occurs in the high bulk flow velocity cases and consequently, the $\mathcal{R}_R$ values increase. Additionally, as the bulk flow velocity increases for cases A–E, larger differences in the interaction rates are present in FOV I. For these cases, dual-flames show lower interaction rates compared with single-flames. Finally, the values of $\mathcal{R}_R$ for both single- and dual-flames generally decrease as a function of downstream distance. This decrease is a result of the change in the type of interaction with downstream distance. Further downstream, attached-flame interactions become less common and larger pocket formation events become more common.

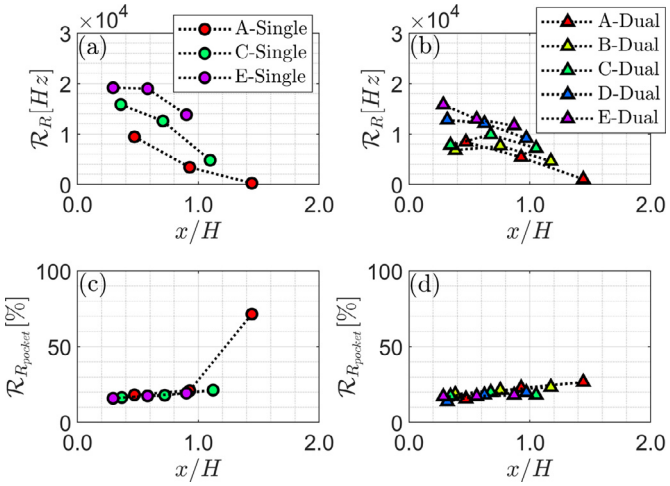

Fig. 9. Reactant-side attached flame–flame interaction rates in 1/ms for (a) single- and (b) dual-flame configurations with variations in bulk flow velocities. Pocket formation rates in [%] from these interactions for (c) single- and (d) dual-flame configurations.

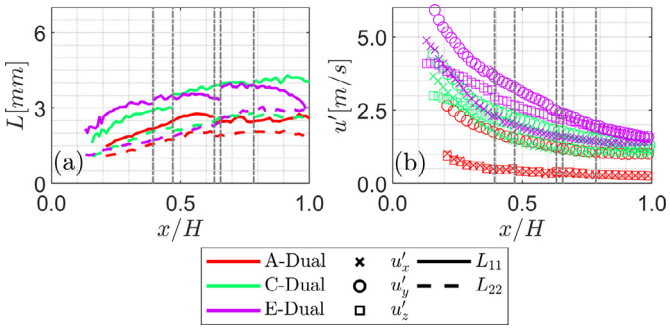

Fig. 10. (a) Turbulence integral length-scales (L_{11} and L_{22}) and (b) intensities along $\bar{c}$=0.5 as functions of downstream distance for dual-flame case A, C, and E. The vertical gray-lines demarcate FOVs II and FOV III for these cases.

Figure 9(c) and (d) shows the percentage of reactant-side interaction events that lead to pocket formation ($\mathcal{R}_{R_{pocket}}$[%]) for cases A–E. For the single-flame cases, this percentage falls in the range of 15–22%, except for FOV III in case A. The high value (72%) for this case is attributed to the large number of flame pinch-off events. The imaging FOV in this region is not sufficiently tall to capture the motion of the flame tip in all cases, resulting in incomplete identification of the locations of flame pinching that leads to large-scale pocket formation. This lack of information results in missing interaction events for this region, leading to the low count of attached interactions. The percentage of reactant gas pockets formed in the dual-flame cases fall in the range of 13–27%. These results show that for both flame configurations, the number of interactions leading to reactant-gas pocket formations increases as the downstream distance increases.

Figure 10 shows the turbulence length- and velocity-scales along the $\bar{c}=0.5$ contour as functions of downstream distance for the dual-flame cases A, C, and E. As shown in Fig. 10(a), L_{11} and L_{22} increase near the flame along the downstream direction and this increase in the turbulence scales likely increases the amount of wrinkling along the flame front. This enhanced wrinkling results in a higher probability of pocket formation rather than cusp burnout as the flame structure is highly curved. Additionally, the turbulence velocity-scales decay as a function of downstream distance near the flame, indicating that large velocity fluctuations result in more cusp burnout interactions and large integral length-scales result in more pocket-forming interactions.

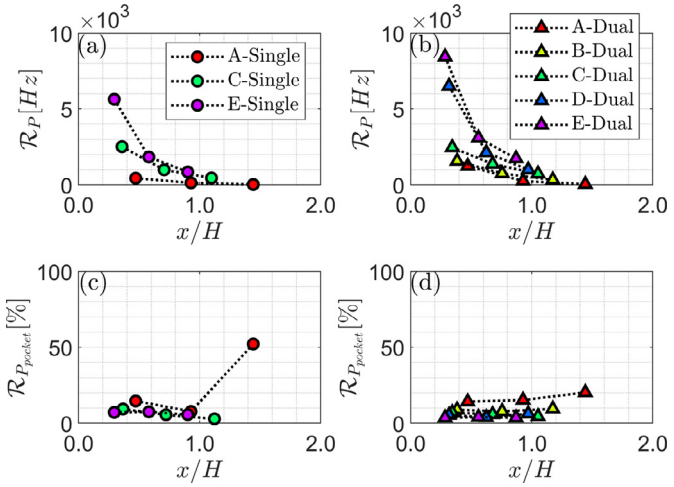

Fig. 11. Product-side attached flame–flame interaction rates in 1/ms for (a) single- and (b) dual-flame configurations with variations in bulk flow velocities. Pocket formation rates in [%] from these interactions for (c) single- and (d) dual-flame configurations.

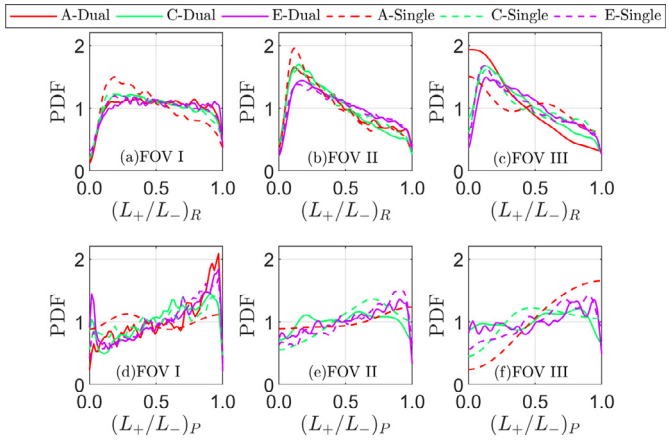

Fig. 12. PDFs of $(L_+/L_-)_R$ and $(L_+/L_-)_P$; L_-corresponds to the arc-length of the flame to be consumed before an interaction event and L_+ corresponds to the arc-length of the remaining local flame structure after the interaction event. Reactant-side interaction results shown in (a) FOV I, (b) FOV II, and (c) FOV III. Product-side interaction results shown in (d) FOV I, (e) FOV II, and (f) FOV III.

Figure 11 shows the rates of product-side interactions ($\mathcal{R}_P$) for the same cases as Fig. 9. Like $\mathcal{R}_R$, $\mathcal{R}_P$ decreases with downstream distance and higher velocity cases lead to higher values of $\mathcal{R}_P$ for both single- and dual-flame cases. Increasing bulk flow velocity increases the local turbulence level, which allows for the possibility of local turbulence to overcome flame propagation, resulting in higher rates of product-side interactions. Additionally, larger differences are present in FOV I for all cases; these differences become smaller farther downstream as the turbulence intensity decays. Figure 11(c) and (d) shows percentages of pocket formations from identified product-side interactions; these percentages are in the range of 1–15% and 3–20% for single- and dual-flames, respectively. In the case of product-side interactions, the percentage of interactions leading to formation of flame pockets decreases as the bulk flow velocity increases. This is observed for both single- and dual-flame configurations. While the increase in integral length-scales facilitates pocket-forming along the downstream direction in the case of reactant-side interactions, it does not promote pocket formation in the case of product-side interactions. The interaction rate behaviors in Figs. 9 and 11 are similar for single- and dual-flame configurations. The reactant-side interaction rates are generally higher than the product-side interaction rates. This finding is consistent with results from DNS studies [22,23,32]. However, differences exist between the absolute rate values between the two configurations. For dual-flames, $\mathcal{R}_R$ values are smaller, and $\mathcal{R}_P$ values are larger when compared with single-flames. It is likely that the presence of adjacent interacting flowfields alters the mean shear in the case of dual-flames that can change the local flow dynamics and impact the local flame–flame interaction statistics [54]; this interaction is absent in the single-flame cases.

The measurement techniques employed in this study are limited to imaging the in-plane components of flame–flame interactions. As flame–flame interactions are inherently three-dimensional, it is necessary to rigorously estimate the effect of through-plane velocity and flame surface orientation [42]. While exact quantification of these uncertainties may require full three-dimensional measurements of the flame surface, we provide an estimate of the out-of-plane fluid motion at the interaction locations using s-PIV measurements. To estimate which interaction is real rather than the result of a three-dimensional motion, we assume that if the out-of-plane velocity is less than the turbulent flame speed (as defined by $S_T = s_L\ (1 + (u'/s_L)^2)^{1/2}$), then the interaction is likely real. Using this metric, we estimate that 92% of the interactions in case A and 82% in case E are real. This current methodology for estimating the uncertainty is discussed in detail in the supplementary material; higher fidelity methods are being continually developed to provide a more robust way of quantifying uncertainties from three dimensional affects. The out-of-plane flame orientation and propagation are currently not accounted for in the analysis and will be considered in future work.

3.4. Topology of flame–flame interactions

3.4.1. Flame surface annihilation

In turbulent flames, flame–flame interactions lead to flame area annihilation, which is an important marker for fluctuations in local burning velocity, flame stretch, and local heat release rate [24,26,28–30,34–41]. To quantify fluctuations in local flame surface due to interactions, the arc-lengths of consumed and remaining flame lengths (L_- and L_+) from flame–flame interaction events are calculated and compared by tracing edges of registered binarized OH-PLIF images, as described in Section 2.2.3. Relative flame surface annihilation is calculated as (L_+/L_-), where L_- is the consumed flame arc-length from the interaction event and L_+ is the remaining flame arc-length. This relative value corresponds to the amount of flame surface annihilation occurring due to a flame–flame interaction event. This analysis closely ties with the goal of informing a model for FSD destruction. Figure 12 shows the probability density functions (PDFs) of these relative annihilation lengths in single- and dual-flames for both reactant-side and product-side interactions. The PDFs of $(L_+/L_-)_R$ from reactant-side interactions in sub-figures (a), (b), and (c) show that relative surface annihilations occur over a wide range of length-scales. In FOV I, the PDFs for high velocity cases C and E are nearly uniform for $(L_+/L_-)_R$=0.1-0.9. This implies that a majority of the local flame surface destruction due to reactant-side interactions falls in a broad range of 10–90%. The PDF plot for single-flame case A shows a peak near $(L_+/L_-)_R$=0.15, which implies that the most probable flame surface annihilation results in an 85% destruction of the local flame surface. For larger downstream distances (FOV II and III), all single- and dual-flame cases show a peak in the range of 0.10–0.15 for the PDF plots, where the most probable flame surface destruction is 85–90% of the local flame surface. These PDF plots indicate that variations in bulk flow velocities do not significantly alter the relative amount of flame surface annihilation due to reactant-side interactions.

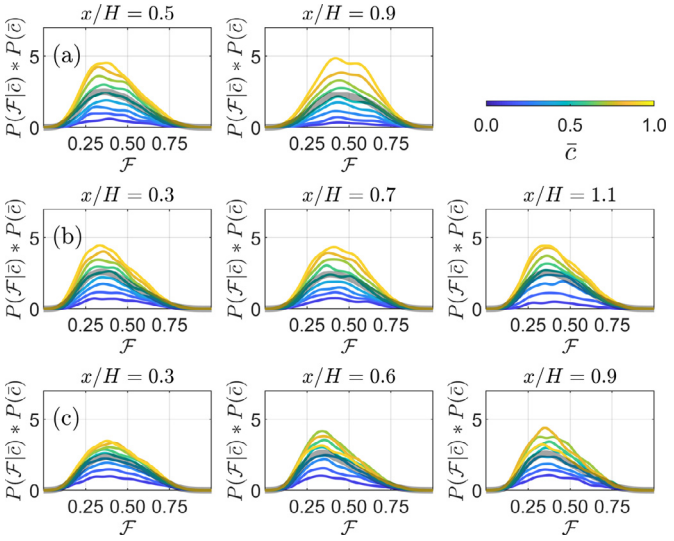

Fig. 13. PDFs of $\mathcal{F}$ of reactant-side interactions conditioned on $\bar{\boldsymbol{c}}$ values of 0.1–0.9 for dual-flame: (a) case A, (b) case C, and (c) case E. x/H labels represent the mid-location of each FOV. FOV III for case A does not have enough data to calculate PDFs conditioned on $\bar{\boldsymbol{c}}$. Thick transparent gray lines indicate the unconditioned PDF of $\mathcal{F}$. The color bar represents values of $\bar{c}$.

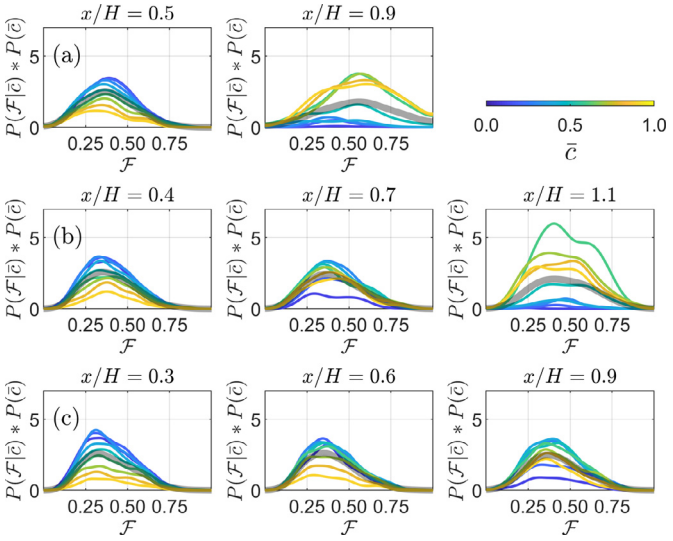

Fig. 14. PDFs of $\mathcal{F}$ of product-side interactions conditioned on $\bar{\boldsymbol{c}}$ values of 0.1–0.9 for single-flame: (a) case A, (b) case C, and (c) case E. x/H labels represent the mid-location of each FOV. FOV III for case A does not have enough data to calculate PDFs conditioned on $\bar{\boldsymbol{c}}$. Thick transparent gray lines indicate the unconditioned PDF of $\mathcal{F}$. The color bar represents values of $\bar{c}$.

PDFs of $(L_+/L_-)_P$ from product-side interactions are shown in sub-figures (d)–(f). For all cases in both flame configurations, PDFs peak near 0.8–0.9, suggesting that the relative amount of flame surface annihilation is quite small compared to the local flame surface undergoing a reactant-side interaction event. Combined with the interaction rates in Fig. 11, these results indicate that product-side interactions are a relatively small contribution to flame surface annihilation. Comparison between single- and dual-flames shows differences, however, with no obvious trends due to changes in bulk flow velocities. The differences that exist in these PDFs may be a result of the differences in the flowfields and global flame behavior of the two configurations in the interacting regions. In the dual-flames case, flame bending is observed for both FOVs II and III, indicating more flow interaction that impacts the amount of mean shear and dynamics of the flame front. As a result, flame front wrinkling and flame annihilation events can be quite different between these configurations in this region.

3.4.2. Flame annihilation shapes

As discussed in Section 3.4.1, flame surface annihilations occur over a range of scales for reactant- and product-side interactions. Quantifying the shapes of flame–flame interactions using filamentarity ($\mathcal{F}$) can provide insights into the most common types of interactions occurring in the flames investigated in this study. These shapes can also help elucidate the role of local turbulence in the occurrence of flame–flame interactions for the future development of FSD annihilation models. Figure 13 shows probabilities of $\mathcal{F}$ of reactant-side interaction shapes for dual-flame cases A, C, and E, conditioned on time-averaged progress variable, $P(\mathcal{F}|\bar{c}) * P(\bar{c})$. The $\bar{c}$ value for an interaction is extracted at the centroid location of the interaction shape. The conditioned PDFs of $\mathcal{F}$ are created using a bivariate Gaussian density estimator that estimates the joint-PDFs (J-PDFs) between two independent variables [55]. The $P(\mathcal{F}|\bar{c}) * P(\bar{c})$ show higher probabilities of reactant-side interactions occurring at $\bar{c}$ closer to 1. This observation holds true for all FOVs, as shown in Fig. 13. These PDFs have a wide distribution in filamentarity and the peaks at various $\bar{c}$ values generally fall in the range of $\mathcal{F}$=0.3–0.5, indicating that the interactions typically have an elliptical shape with a major-to-minor axis ratio in the range of 4–7. Conditioned PDFs of $\mathcal{F}$ of reactant-side interactions

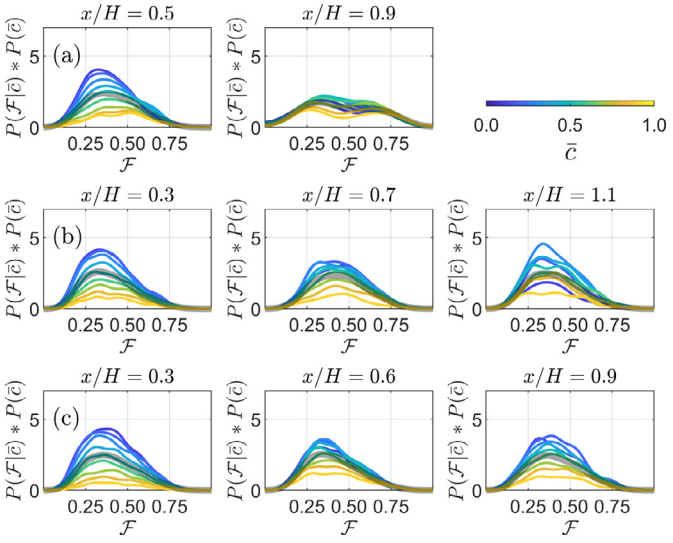

Fig. 15. PDFs of $\mathcal{F}$ of product-side interactions conditioned on $\bar{\boldsymbol{c}}$ values of 0.1–0.9 for dual-flame: (a) case A, (b) case C, and (c) case E. x/H labels represent the mid-location of each FOV. FOV III for case A does not have enough data to calculate PDFs conditioned on $\bar{\boldsymbol{c}}$. Thick transparent gray lines indicate the unconditioned PDF of $\mathcal{F}$. The color bar represents values of $\bar{c}$.

for single-flames have very similar distributions to those shown for dual-flames in Fig. 13 and are not included here. The similarity in these conditioned PDFs of $\mathcal{F}$ for single- and dual-flames shows that despite large differences in the magnitudes of $\mathcal{R}_R$ between the two configurations, the interaction topologies and locations in the flame brush do not vary significantly.

Figures 14 and 15 show the $\bar{c}$ conditioned PDFs of $\mathcal{F}$ for product-side interactions of single- and dual-flames. In both configurations, higher probabilities of product-side interactions exist at $\bar{c}$ closer to 0 in FOV I. The conditioned PDFs show a wide distribution for $\mathcal{F}$, showing that product-side interactions can also occur at a range of shapes. These conditional PDFs peak for a range of $\mathcal{F} = 0.3–0.5$ for both single- and dual-flames in FOV I. Although values of $\mathcal{R}_P$ can be different between single- and dual-flames, their topology remains similar in the FOV I between the

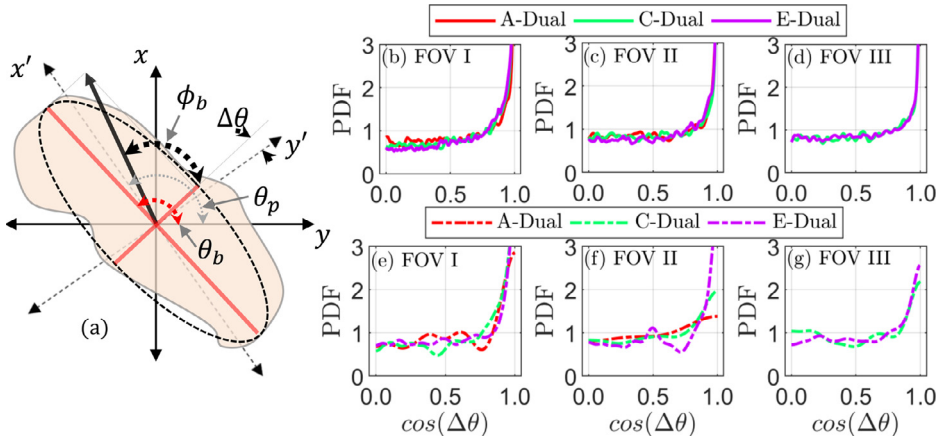

Fig. 16. (a) Schematic of the orientation of flame interaction shape, principal plane of strain rates with respect to the Cartesian coordinate frame. Comparison of PDFs of the alignment between the major axis of the flame–flame interaction shape (θ_b) and the principal angles of the strain rates (θ_p). Reactant-side interaction statistics are shown in (b) FOV I, (c) FOV II, and (d) FOV III; product-side interaction statistics are shown in (e) FOV I, (f) FOV II, and (g) FOV III.

two configurations, likely because of weak interaction between the flowfields. There are significant differences in the most probable $\mathcal{F}$ value at various $\bar{c}$ in FOV II. For single-flame cases A and C, higher $\bar{c}$ values ($\bar{c}$>0.3) show higher probabilities compared with lower $\bar{c}$ values, indicating that higher probabilities of product-side interactions shift location in the flame brush. Additionally, the peaks of the PDFs shift toward higher values of filamentarity ($\mathcal{F} \geq 0.5$) in single-flame case A, implying the occurrence of unidirectional stretching of the product-side interaction topologies. PDF plots for single-flame case E in FOV II follow those from FOV I and peak at similar values of $\mathcal{F}$. In FOV II, the distribution of interactions is somewhat evenly spread in $\bar{c}$ space for dual-flames case A. The probabilities still show a peak in the range of $\mathcal{F}$=0.3–0.5; however, the distribution is wide. PDF distributions in FOV II remain similar to FOV I in the case of dual-flames C and E. Finally, comparisons in FOV III between single- and dual-flames case C show that for the single-flame configuration, the maximum probability occurs for $\bar{c}$ ∼0.6, whereas in the dual-flame configuration, maximum probabilities still occur near the reactant-side of the flame brush in the range of $\bar{c}$=0.3–0.4. For both configurations of case E, the PDF plots in FOV III show that most interactions are still occurring near the reactant-side of the flame brush, with peaks for $\mathcal{F}$=0.3–0.5. These PDF plots suggest that most of the interactions occur in the $\bar{c}$ ranges of 0.3–0.5 for these flames

The major-to-minor axis ratio of a flame–flame interaction shape can be obtained by fitting the shape with an ellipse that has the same normalized second central moments as that of the shape. The ratio of these axes can then be compared to the ratio of the turbulence length-scales (L_{11}/L_{22}) near the flame. This comparison can link the scales of turbulence to that for flame surface annihilation of flame surface. The interaction shape axis ratio values obtained from this method fall in the range of 1.5–2.0 and the values of L_{11}/L_{22} peak near 1.5–1.8 for various downstream locations. Turbulent eddies with this oblong shape can affect the morphology of the flame structure and likely drive the shape of flame–flame interactions. Additionally, we can consider the local orientation of these interactions to the principal orientations of the local strain rates to understand the link between the local strain and flame–flame interactions.

3.4.3. Flame annihilation orientations

Filamentarity results presented in the previous section describe the shape of flame–flame interactions. Comparisons between the orientations of these shapes and the local strain field can provide some insights into how turbulence drives the individual interaction events. We determine the orientation of the interaction shape by fitting it with an ellipse. Major axes of the fitted ellipses are identified to find the local angles (θ_b) formed between these axes and the Cartesian y-axis, as shown in Fig. 16(a). Using this formulation, the orientation of a majority of reactant- and products-side flame–flame interactions are found to be near 0° and 180°. This implies that many of the interaction events occur in the direction of the bulk flow. To assess the alignment of the interaction shape with the local strain field, we calculate the principal axes of strain and compare them to the axes of the ellipse. The principal angles (θ_p) of the local strain rates are obtained using Equation (4),

$$\theta_p = \frac{1}{2}\cdot\tan^{-1}\left(\frac{2S_{12}}{S_{11}-S_{22}}\right); S_{12} = \frac{1}{2}\left(\frac{\partial U_x}{\partial y}+\frac{\partial U_y}{\partial x}\right),$$
$$S_{11} = \frac{\partial U_x}{\partial x}, S_{22} = \frac{\partial U_y}{\partial y} \quad (4)$$

where, S_{12} is the shear strain rate, while S_{11} and S_{22} are the compression/elongation strain rates in x- and y-directions. The alignment between θ_b and θ_p can show the relative alignment of the flame–flame interaction shape and the local strain as the interaction event occurs. Both θ_p and θ_b are measured in [0°, +180°] and the differences between these angles are reported as $\Delta\theta$. Cosines of $\Delta\theta$ quantify the alignment between θ_b and θ_p and fall in [0, +1], with perfect alignment at +1, and misalignment at 0.

Figure 16(b)–(g) shows the PDFs of cosines of $\Delta\theta$ for dual-flame cases A, C, and E in all three FOVs. These PDF plots show that the most probable value of the cosine of $\Delta\theta$ is +1, indicating that the directions of the most extensive and the most compressive strain rates align with the directions of the major and minor axes of the flame–flame interaction shapes, indicating that compressive forces in the local flowfield lead to the merging or pinch-off of the flame fronts for these flame–flame interactions.

4. Conclusions

In this study, high-speed OH-PLIF and s-PIV are used to study the effect of interacting flames on the local topology of flame fronts and statistics conditioned on local flame front reduction events are presented. With the aid of an image registration technique, dynamics of flame–flame interactions are tracked to capture these broad-range scale interactions. Comparisons between single- and dual-flame configurations show that higher rates of reactant-side interactions occur in single-flame configurations compared to the dual-flames, and vice-versa for product-side interactions. In both configurations, reactant-side interactions are more likely to

occur than product-side interactions and the alignment between the orientation of principal strain rates at the locations of interactions and the shape of the interactions shows that the local compressive strain rates are the physical driving forces behind local flame annihilation events. Reactant-side interactions in these flames have larger flame surface annihilations compared with product-side interactions as larger product-side flame surface annihilations would require much stronger compressive forces in the flowfield to dominate flame kinematics. Filamentarity is used to categorize and quantify the shapes of interactions and PDFs show the existence of a wide range of shapes for both types of interactions. Finally, it is found that local turbulence can morph these interactions shapes.

Results presented in this study stem from two-dimensional measurements and while the three-dimensional flame dynamics can influence these results, we utilize the simultaneous out-of-plane component of velocity to reasonably quantify the uncertainties involved in this procedure. The implications of results presented in this study are three-fold: (1) how the frequency of flame–flame interactions changes for different operating conditions and at different locations along the flame, (2) what is the most probable flame surface destruction due interaction events, and (3) what is the link between the local turbulence scales vs. the interaction shapes and the orientation of the shapes vs. the principal strain angles. These results from this study can be utilized as a first attempt towards developing an advanced physics-based sub-grid scale flame surface destruction model for performing high-fidelity simulations. Distributions of turbulence scales, along with interaction frequency and orientations could be used to obtain a probabilistic model for the surface destruction term to be implemented in the FSD transport term. Other efforts can be put towards developing a mathematical model, which also captures the physical processes driving these interaction events. Flame–flame interaction rates presented in this study can be utilized to validate modeling of the surface destruction term in the flame surface density equations for sub-grid scale models. Recommendations for future work include multi-species and temperature measurements to understand how mixing can impact these interaction events.

Acknowledgments

This work was supported by the Air Force Office of Scientific Research under Grants FA9550-16-1-0044 and FA9550-16-1-0075 with program manager Dr. Chiping Li. The authors would like to acknowledge Dr. Campbell Carter at the AFRL for providing equipment support for performing these experiments.

Supplementary material

Supplementary material associated with this article can be found, in the online version, at doi:10.1016/j.combustflame.2019.02.006.

References

[1] J. Samarasinghe, S. Peluso, M. Szedlmayer, A. De Rosa, B. Quay, D. Santavicca, Three-dimensional chemiluminescence imaging of unforced and forced swirl-stabilized flames in a lean premixed multi-nozzle can combustor, J. Eng. Gas Turbines Power 135 (10) (2013) 101503.
[2] N.A. Worth, J.R. Dawson, Cinematographic OH-PLIF measurements of two interacting turbulent premixed flames with and without acoustic forcing, Combust. Flame 159 (3) (2012) 1109–1126.
[3] N.A. Worth, J.R. Dawson, Tomographic reconstruction of OH* chemiluminescence in two interacting turbulent flames, Meas. Sci. Technol. 24 (2) (2012) 024013.
[4] J.R. Dawson, N.A. Worth, Flame dynamics and unsteady heat release rate of self-excited azimuthal modes in an annular combustor, Combust. Flame 161 (10) (2014) 2565–2578.
[5] M. Aguilar, M. Malanoski, G. Adhitya, B. Emerson, V. Acharya, D. Noble, T. Lieuwen, Helical flow disturbances in a multinozzle combustor, J. Eng. Gas Turbines Power 137 (9) (2015) 091507.
[6] T.E. Smith, I.P. Chterev, B.L. Emerson, D.R. Noble, T.C. Lieuwen, Comparison of single-and multinozzle reacting swirl flow dynamics, J. Propuls. Power 34 (2) (2017) 1–11.
[7] U. Hegde, D. Reuter, B. Zinn, Sound generation by ducted flames, AIAA J. 26 (5) (1988) 532–537.
[8] D. Reuter, U. Hegde, B. Zinn, Flowfield measurements in an unstable ramjet burner, J. Propuls. Power 6 (6) (1990) 680–685.
[9] R. Tacina, C.-P. Mao, C. Wey, Experimental investigation of a multiplex fuel injector module for low emission combustors, 41st Aerospace Sciences Meeting and Exhibit (2003), p. 827.
[10] D. Fanaca, P. Alemela, C. Hirsch, T. Sattelmayer, Comparison of the flow field of a swirl stabilized premixed burner in an annular and a single burner combustion chamber, J. Eng. Gas Turbines Power 132 (7) (2010) 071502.
[11] W.Y. Kwong, A.M. Steinberg, Blowoff and reattachment dynamics of a linear multinozzle combustor, J. Eng. Gas Turbines Power 141 (1) (2019) 011015.
[12] E. Machover, E. Mastorakos, Experimental investigation on spark ignition of annular premixed combustors, Combust. Flame 178 (2017) 148–157.
[13] J. Samarasinghe, W. Culler, B.D. Quay, D.A. Santavicca, J. O'Connor, The effect of fuel staging on the structure and instability characteristics of swirl-stabilized flames in a lean premixed multinozzle can combustor, J. Eng. Gas Turbines Power 139 (12) (2017) 121504.
[14] J. Kariuki, N. Worth, J. Dawson, E. Mastorakos, Visualisation of blow-off events of two interacting turbulent premixed flames, 51st AIAA Aerospace Sciences Meeting including the New Horizons Forum and Aerospace Exposition (2013), p. 692.
[15] S. Chung, J. Kim, C. Law, Extinction of interacting premixed flames: theory and experimental comparisons, Symp.(Int.) Combust. 21 (1988) 1845–1851.
[16] C. Chen, S. Sohrab, Upstream interactions between planar symmetric laminar methane premixed flames, Combust. Flame 101 (3) (1995) 360–370.
[17] H.G. Im, J.H. Chen, Preferential diffusion effects on the burning rate of interacting turbulent premixed hydrogen-air flames, Combust. Flame 131 (3) (2002) 246–258.
[18] J. Park, T. Echekki, LES–ODT study of turbulent premixed interacting flames, Combust. Flame 159 (2) (2012) 609–620.
[19] B. Ranganath, T. Echekki, Effects of preferential and differential diffusion on the mutual annihilation of two premixed hydrogen–air flames, Combust. Theory Model. 9 (4) (2005) 659–672.
[20] B. Ranganath, T. Echekki, On the role of heat and mass transport during the mutual annihilation of two premixed propane–air flames, Int. J. Heat Mass Transf. 49 (25-26) (2006) 5075–5080.
[21] S. Sohrab, Z. Ye, C. Law, An experimental investigation on flame interaction and the existence of negative flame speeds, Symp. (Int.) Combust. 20 (1985) 1957–1965.
[22] T. Dunstan, N. Swaminathan, K. Bray, N. Kingsbury, Flame interactions in turbulent premixed twin V-flames, Combust. Sci. Technol. 185 (1) (2013) 134–159.
[23] T. Dunstan, N. Swaminathan, K. Bray, N. Kingsbury, The effects of non-unity Lewis numbers on turbulent premixed flame interactions in a twin V-flame configuration, Combust. Sci. Technol. 185 (6) (2013) 874–897.
[24] T. Echekki, J.H. Chen, I. Gran, The mechanism of mutual annihilation of stoichiometric premixed methane-air flames, Symp. (Int.) Combust. 26 (1996) 855–863.
[25] T. Echekki, J.H. Chen, Unsteady strain rate and curvature effects in turbulent premixed methane-air flames, Combust. Flame 106 (1-2) (1996) 184–202.
[26] W. Kollmann, J.H. Chen, Pocket formation and the flame surface density equation, Symp. (Int.) Combust. 27 (1998) 927–934.
[27] C. Sun, C. Law, On the consumption of fuel pockets via inwardly propagating flames, Symp. (Int.) Combust. 27 (1998) 963–970.
[28] J.H. Chen, T. Echekki, W. Kollmann, The mechanism of two-dimensional pocket formation in lean premixed methane-air flames with implications to turbulent combustion, Combust. Flame 116 (1-2) (1999) 15–48.
[29] N. Fogla, F. Creta, M. Matalon, Effect of folds and pockets on the topology and propagation of premixed turbulent flames, Combust. Flame 162 (7) (2015) 2758–2777.
[30] A.N. Lipatnikov, J. Chomiak, V.A. Sabelnikov, S. Nishiki, T. Hasegawa, Unburned mixture fingers in premixed turbulent flames, Proc. Combust. Inst. 35 (2015) 1401–1408.
[31] H. Tsuji, I. Yamaoka, Structure and extinction of near-limit flames in a stagnation flow, Symp. (Int.) Combust. 19 (1982) 1533–1540.
[32] R. Griffiths, J. Chen, H. Kolla, R. Cant, W. Kollmann, Three-dimensional topology of turbulent premixed flame interaction, Proc. Combust. Inst. 35 (2015) 1341–1348.
[33] J.R. Osborne, S.A. Ramji, C.D. Carter, S. Peltier, S. Hammack, T. Lee, A.M. Steinberg, Simultaneous 10kHz TPIV, OH PLIF, and CH_2O PLIF measurements of turbulent flame structure and dynamics, Exp. Fluids 57 (5) (2016) 65.
[34] R. Prasad, J. Gore, An evaluation of flame surface density models for turbulent premixed jet flames, Combust. Flame 116 (1-2) (1999) 1–14.
[35] C. Meneveau, T. Poinsot, Stretching and quenching of flamelets in premixed turbulent combustion, Combust. Flame 86 (4) (1991) 311–332.
[36] J. Duclos, D. Veynante, T. Poinsot, A comparison of flamelet models for premixed turbulent combustion, Combust. Flame 95 (1-2) (1993) 101–117.
[37] D. Veynante, J.M. Duclos, J. Piana, Experimental analysis of flamelet models for premixed turbulent combustion, Symp. (Int.) Combust. 25 (1994) 1249–1256.

[38] E. Hawkes, R. Cant, A flame surface density approach to large-eddy simulation of premixed turbulent combustion, Proc. Combust. Inst. 28 (2000) 51–58.
[39] K.N.C. Bray, Studies of the turbulent burning velocity, Proc. R. Soc. Lond. A 431 (1882) (1990) 315–335.
[40] S.M. Candel, T.J. Poinsot, Flame stretch and the balance equation for the flame area, Combust. Sci. Technol. 70 (1-3) (1990) 1–15.
[41] S.A. Filatyev, J.F. Driscoll, C.D. Carter, J.M. Donbar, Measured properties of turbulent premixed flames for model assessment, including burning velocities, stretch rates, and surface densities, Combust. Flame 141 (1-2) (2005) 1–21.
[42] A.W. Skiba, T.M. Wabel, C.D. Carter, S.D. Hammack, J.E. Temme, T. Lee, J.F. Driscoll, Reaction layer visualization: a comparison of two PLIF techniques and advantages of kHz-imaging, Proc. Combust. Inst. 36 (2017) 4593–4601.
[43] P.E. Roach, The generation of nearly isotropic turbulence by means of grids, Int. J. Heat Fluid Flow 8 (2) (1987) 82–92.
[44] N. Peters, Turbulent combustion, Cambridge University Press, 2000.
[45] F. Picano, F. Battista, G. Troiani, C.M. Casciola, Dynamics of PIV seeding particles in turbulent premixed flames, Exp. Fluids 50 (1) (2011) 75–88.
[46] R.C. Gonzalez, R.E. Woods, Digital image processing, Prentice Hall, Upper Saddle River, NJ, 2002.
[47] H. Chen, N. Kingsbury, Efficient registration of nonrigid 3-D bodies, IEEE Trans. Image Process. 21 (1) (2012) 262–272.
[48] N. Kingsbury, Complex wavelets for shift invariant analysis and filtering of signals, Appl. Comput. Harmon. Anal. 10 (3) (2001) 234–253.
[49] J.P. Thirion, Image matching as a diffusion process: an analogy with Maxwell's demons, Med. Image Anal. 2 (3) (1998) 243–260.
[50] T. Vercauteren, X. Pennec, A. Perchant, N. Ayache, Diffeomorphic demons: efficient non-parametric image registration, Neuroimage 45 (1) (2009) S61–S72.
[51] S.B. Pope, Turbulent flows, IOP Publishing, 2001.
[52] S. Bharadwaj, V. Sahni, B.S. Sathyaprakash, S.F. Shandarin, C. Yess, Evidence for filamentarity in the Las Campanas redshift survey, Astrophys. J. 528 (1) (2000) 21.
[53] J.F. Driscoll, Turbulent premixed combustion: flamelet structure and its effect on turbulent burning velocities, Prog. Energy Combust. Sci. 34 (1) (2008) 91–134.
[54] A. Tyagi, I. Boxx, S. Peluso, J. O'Connor, The role of flow interaction in flame—flame interaction events in a dual burner experiment, Proc. Combust. Inst. 37 (2) (2019) 2485–2491.
[55] B.W. Silverman, Density estimation for statistics and data analysis, Routledge, 2018.